Characterizing point-source carbon emissions by combining TROPOMI CO and OCO CO_2 data.

Gijs Leguijt[1,2], Joannes D. Maasakkers[1], Hugo A.C. Denier van der Gon[2], Arjo J. Segers[2], Hannah Nesser[3], and Ilse Aben[1,4]

[1]SRON Netherlands Institute for Space Research, Leiden, the Netherlands
[2]Department of Air Quality and Emissions Research, Netherlands Organisation for Applied Scientific Research, TNO, Utrecht the Netherlands
[3]Jet Propulsion Laboratory, California Institute of Technology, California, United States of America
[4]Department of Earth Sciences, Vrije Universiteit Amsterdam, Amsterdam, the Netherlands

July 30, 2025

Abstract

Understanding and independently validating carbon emissions from concentrated point sources is vital to support climate policy. Satellite-based quantifications of CO_2 point source emissions have been limited by the spatial coverage of current satellite instruments. We combine three different satellite instruments to determine carbon monoxide (CO) and carbon dioxide (CO_2) emissions of seven large cities and six industrial complexes. We first estimate CO emission rates using TROPOMI CO observations with the Cross-Sectional Flux method. Subsequently, CO_2 emission rates are calculated by multiplying with the ratio of TROPOMI-observed CO enhancements and CO_2 enhancements from OCO-2 and OCO-3, also representing the combustion efficiency. We use synthetic observations to validate our approach and show that the inclusion of TROPOMI CO observations increases the number of possible CO_2 emission quantifications. Using 2018-2023 observations, we find lower CO emission rates for Delhi and Lahore than the EDGAR emission inventory. In contrast, our CO emission estimates exceed bottom-up inventory estimates for most industrial sources. This is caused by observed combustion efficiencies that are generally lower than those reported in emission inventories. Our CO_2 emission estimates show better agreement with EDGAR than the CO emissions, especially for industrial sources. We find higher CO_2 emission rates than EDGAR for the cities of Delhi, Lahore, and Cairo that better agree with the ODIAC inventory. Our work shows the importance of CO as a co-emitted species, and paves the way for a similar approach to be applied to the combination of TROPOMI, its successor Sentinel-5, and the future CO2M satellites.

1 Introduction

CO_2 is the most important anthropogenic greenhouse gas. Because of human activity, its concentration has been rising at unprecedented speed over the last century. As a result, temperatures have risen, the ocean has acidified, and natural disasters have become more frequent, leaving few ecosystems untouched (Intergovernmental Panel on Climate Change (IPCC), 2023). To limit the effect of humankind on the Earth system, and in particular the Earth's temperature, the Paris agreement was formulated and signed by almost two hundred parties. This agreement aims to reduce the emissions of greenhouse gases and tries to limit temperature rise to 1.5-2 °C with respect to pre-industrial levels (Horowitz, 2016). Reduction of CO_2 emissions from the largest industries is required to reach this goal and monitoring of current emissions has been identified as a key prerequisite (Intergovernmental Panel on Climate Change (IPCC), 2023). Carbon monoxide (CO) is the product of incomplete combustion and emitted alongside CO_2. As such, estimation of CO and CO_2 emissions allows for the determination of combustion efficiencies, highlighting sources with potential for CO_2 emission reduction. In this work, we show how we combine satellite measurements of CO and CO_2 to quantify emissions and combustion efficiencies of large CO_2 sources.

Satellites have demonstrated to be capable of monitoring greenhouse gas emissions at a range of spatial scales (for example: Houweling et al. (2015); Plant et al. (2022); Chen et al. (2022); Wang et al. (2022); Wilmot et al. (2024); Scarpelli et al. (2024)). It is, however, specifically challenging to measure CO_2 total column concentrations accurately enough from space, as its long atmospheric residence time results in large background concentrations which obscure the signals from individual sources. Nevertheless, the two Orbiting Carbon Observatory instruments (OCO-2 Eldering et al. (2017) and OCO-3 Eldering et al. (2019)) and the Greenhouse gases Observing SATellites (GOSAT and GOSAT-2, Imasu et al. (2023)) are able to measure CO_2 down to the Earth's surface from space. Additionally, the high-spatial-resolution Earth Surface Mineral Dust Source Investigation (EMIT, Green et al. (2023)) instrument has been shown capable of detecting CO_2 enhancements from the largest and most concentrated CO_2 sources (Thorpe et al., 2023; Nelson et al., 2024). Yet, it remains difficult to use them to estimate the CO_2 emission rates of point sources due to their spatial resolution (GOSAT-2), limited sensitivity (EMIT), and limited coverage (OCO). The TROPOMI instrument on ESA's Sentinel-5 Precursor satellite does not measure CO_2 but it provides CO and NO_2 observations with daily global coverage down to a resolution of 7 x 5.5 km^2 for CO (Borsdorff et al., 2018). Both NO_2 and CO are co-emitted with CO_2 for processes including steel production, coal-based power generation, and transport using combustion engines. CO is a product of incomplete combustion, so the combination of CO and CO_2 observations can therefore be used to estimate combustion efficiencies. Various studies using satellite data have shown how co-emitted species can help provide information about CO_2. In particular, NO_2 has been extensively used as a proxy for CO_2 emissions due to its short lifetime (order of hours), resulting in clear localized enhanced NO_2 signals in the satellite data (Hakkarainen et al., 2021; Zhang et al., 2023; Yang et al., 2023; Fuentes Andrade et al., 2024). Fewer studies have investigated CO as a co-emitted species, and these studies have often relied on bottom-up inventories to translate enhancements into emission rates (Park et al., 2021; Wu et al., 2022; Ohyama et al., 2024). Space-based observation of CO enhancements is complicated by its longer lifetime than NO_2 (order of weeks to months), which results in higher background concentrations. However, in addition to CO's importance for determining combustion efficiencies, its longer lifetime also ensures it is transported similarly to the long-lived CO_2.

High-emitting sources observable from space include cities and industrial complexes. In cities, there is a large variety of combustion processes (for example domestic cooking and heating, traffic, and small-scale industries), which makes them large sources of both CO and CO_2 emissions, allowing for the exploitation of their co-emitted nature. Power plants (PP) are the highest emitting CO_2 point sources, and are often highly optimized to have high combustion efficiencies. As such, multiple studies have investigated power plants from space and have demonstrated the ability to estimate emission rates from the measured CO_2 concentrations (e.g. Nassar et al. (2021); Guo et al. (2023); Li et al. (2024); Yang et al. (2024); Nelson et al. (2024)). The corresponding CO emission rates are relatively low, and we do not expect to observe clear localized CO signals from space. Integrated iron and steel plants (ISP) emit large amounts of CO through combustion and processing of iron ore. They often have dedicated power plants for their electricity demand. The resulting industrial complexes emit large amounts of both CO and CO_2, while they can be considered point sources on the scale of satellite instruments like TROPOMI and OCO-2/3 (Wu et al., 2022; Leguijt et al., 2025).

We combine the CO concentrations measured at high spatial coverage by TROPOMI with CO_2 observations measured by the OCO-2 and OCO-3 satellite instruments. OCO-2 is in an orbit that is very similar to TROPOMI, resulting in CO and CO_2 observations that are close in time. Additionally, OCO-3 provides targeted measurements which allow for a closer inspection of high-emitting CO_2 sources (Taylor et al., 2020). We show how we can determine combustion efficiencies and carbon emissions from cities and large industrial complexes, without relying on bottom-up information and/or atmospheric modeling. After evaluation and validation of our method using simulated data, we compare our emission estimates for thirteen locations (seven large cities and six industrial complexes) to bottom-up inventories.

2 Data and Methods

To compute CO and CO_2 emission rates of large point-like sources, we use CO observations from TROPOMI (Section 2.1) and CO_2 observations made by OCO-2 and OCO-3 (Section 2.2) from 2018-2023. In Section 2.3, we describe how we combine the two data products on days where they have overlap over the locations of interest to estimate emission rates that we can compare to the emission inventories described in Section 2.4. We introduce our synthetic data in Section 2.5 and describe how we derive the uncertainties on the emission rates in Section 2.6.

2.1 TROPOMI carbon monoxide data product

In October 2017, the ESA Sentinel-5 precursor satellite was launched carrying the TROPOMI instrument. The mission has been operational since May 2018. The satellite is in a sun-synchronous ascending orbit that passes the equator at 13:30 local time. TROPOMI measures different species in our atmosphere, including NO_2, SO_2, O_3, CH_4, HCHO, aerosols, and CO. TROPOMI combines a large swath (2600 km), which provides daily global coverage, with individual measurements of total columns at a resolution down to 7 x 5.5 km^2 (across x along track) for CO (Veefkind et al., 2012). Total column CO concentrations are retrieved using the short-wave infrared CO retrieval (SICOR) algorithm, based on the absorption spectrum of CO at 2305-2385 nm (Borsdorff et al., 2018; Landgraf et al., 2021). The TROPOMI CO total column product is validated using the global ground-based Total Carbon Column Observing Network (TCCON, (Wunch et al., 2011)). A comparison to the unscaled TCCON product yields a mean difference per station of $2.45 \pm 3.38\%$ (Sha et al., 2021).

We use version 2.2.4 of the operational TROPOMI CO product and remove pixels with a TROPOMI Data Quality Value (QA Value) below 0.7, which have limited sensitivity for CO near the surface due to reflection by higher altitude clouds or for which the SICOR algorithm did not converge (Landgraf et al., 2023). Additionally, we remove cloudless pixels (QA Value equal to 1) over water as its low surface albedo results in a lower signal-to-noise ratio.

2.2 OCO carbon dioxide data product

For CO_2 observations, we rely on the OCO-2 and OCO-3 instruments (Eldering et al., 2017, 2019). OCO-2 and OCO-3 are similar instruments, mounted on different platforms. OCO-2 was launched in 2014 on a dedicated satellite in a sun-synchronous orbit very similar to the one of TROPOMI, crossing the equator at 13:36 local time (Taylor et al., 2023). OCO-3 has been mounted on the International Space Station (ISS) since 2019, which means its overpass time varies. Despite the ISS flying at roughly half the altitude of OCO-2, the two instruments have similar spatial resolutions, 1.3x2.25 km^2 and 1.6x2.2 km^2 for OCO-2 and OCO-3 respectively. Both instruments provide eight simultaneous adjacent measurements, which result in a swath of ∼10 km. In addition to continuous single swath normal operation, both OCO instruments can be targeted at specific scenes on Earth to allow for further investigation of specific sites. Targeting of OCO-2 is limited to pre-defined targets, while OCO-3 has more flexibility. OCO-3 has a Snapshot Area Mapping (SAM) mode which measures multiple adjacent swaths over a span of minutes, resulting in dense clusters of pixels spanning a ∼85x85 km^2 region (Taylor et al., 2020).

Like TROPOMI, OCO uses absorption of reflected sunlight to determine total column concentrations. The three bands relevant for CO_2 are the oxygen A-band (around 0.765 μm), the weak CO_2 absorption band (around 1.61 μm), and the strong CO_2 absorption band (around 2.06 μm). The weak and strong CO_2 absorption bands have sensitivity to CO_2 while the oxygen A-band is mainly used to estimate the atmospheric path length (Eldering et al., 2017). We use the bias corrected version 10.4 of both the OCO-2 and OCO-3 XCO_2 total column products. We remove pixels with a quality value of one, and only

use those with a successful retrieval (quality value equal to zero) (Taylor et al., 2023). TCCON is also the reference ground-based network for the validation of space-based XCO_2 total column measurements, and a comparison to TCCON over land shows a single sounding root mean squared error of 1.15 (1.33) ppm for OCO-2 (OCO-3) (Taylor et al., 2023; Chatterjee et al., 2022).

2.3 Two-step method

We use TROPOMI observations to determine Q_{CO}, the CO emission rate. Subsequently, we combine our CO emission rate estimates with the limited spatial coverage of OCO-2 and OCO-3 to determine CO_2 emission rates and combustion efficiencies (the ratio of the CO to CO_2 emission rates).

To determine Q_{CO}, we use the Cross-Sectional Flux (CSF) method as described in Leguijt et al. (2023) by virtue of its speed, independence of prior information, and low computational burden. This mass-balance method is based on the continuity equation and calculates Q_{CO} by integrating CO mass enhancements (Δ[CO]) over transects perpendicular to the plume direction (Varon et al., 2018):

$$Q_{CO} = \int U_{\perp}(x,y)\Delta[CO](x,y)dy. \tag{1}$$

Here, x and y are coordinates along and perpendicular to the plume respectively. Multiplication with an effective wind speed perpendicular to the integral ($U_{\perp}$) gives an emission rate estimate for single plumes. The effective wind is calculated from the 10-m wind speed given by NASA/GMAO GEOS-FP reanalysis data (Molod et al., 2012). Figure 1(a) shows an example of the transects (black) and the location of an upwind background region (white), for a more detailed description of how the transects are drawn and the effective wind is determined we refer to Leguijt et al. (2023).

Under identical transport of CO and CO_2, the measured CO_2 enhancement ($\Delta[CO_2]$, ppm) at a distance x downwind of a source is given by

$$\Delta[CO_2](x) = \Delta[CO](x) \cdot \frac{Q_{CO_2}}{Q_{CO}} \cdot \frac{M_{CO}}{M_{CO_2}}, \tag{2}$$

with Q_X the emission rate of species X, and M_X its molar mass. Or, equivalently, and more applicable to our situation,

$$Q_{CO_2} = Q_{CO} \cdot \frac{\Delta[CO_2](x)}{\Delta[CO](x)} \cdot \frac{M_{CO_2}}{M_{CO}}. \tag{3}$$

Figure 1 shows the locations of the sources studied in this work, as well as examples of CO and CO_2 plumes observed for three of the sources. Similarity in the spatial source-distribution between CO and CO_2 is assured by visual inspection of typical enhancements observed for all sources. Specifically, panel (a) shows CO and CO_2 plumes over Baotou, an industrial complex in China, as observed by TROPOMI and OCO-3. The overpass times for TROPOMI and OCO-3 are only eight minutes apart, and the plumes show very similar shapes and directions. The upper panel in Figure 1a shows the transects of the CSF method which follow the shape of the CO plume. We then use the area covered by both the TROPOMI transects (the plume area, outlined in green in Figure 1a) and by OCO observations (the overlapping area is marked in blue in the middle panel of Figure 1a) to determine the enhancement ratio of CO to CO_2. Partially overlapping pixels are included weighted by the overlapping area. We only consider days with at least five OCO pixels overlapping with the TROPOMI plume area. To determine Q_{CO}, we are not restricted to the TROPOMI pixels overlapping with the OCO measurements, and use the full coverage of the entire CO plume as observed by TROPOMI.

Due to its narrow swath, OCO often has no observations in the CO background region, except for observations that are part of SAMs. Additionally, the longer atmospheric lifetime of CO_2 results in a high natural background. This lowers the signal-to-noise ratio of CO_2 plumes and makes an accurate background determination for OCO even more critical. Therefore, in addition to calculating the background as the mean concentration upwind, we also determine a background for CO and CO_2 by taking the mean concentration in the strips of 0.05°on either side of the plume area; this region is shown in red in the middle panel of Figure 1a. We use this region as the background if there is no upwind CO_2 coverage. Additionally, we use both values in our emission uncertainty estimates, as explained in Section 2.6. Large differences between the two background estimates can indicate potential over- or underestimation of the background concentration, that can, for example, arise from altitude-related biases. To avoid inaccurate background estimates biasing our final emission estimates, we remove days where the difference between the estimated background concentrations exceeds one standard deviation of all pixels within 100 km of the source (the full area shown in Figure 1).

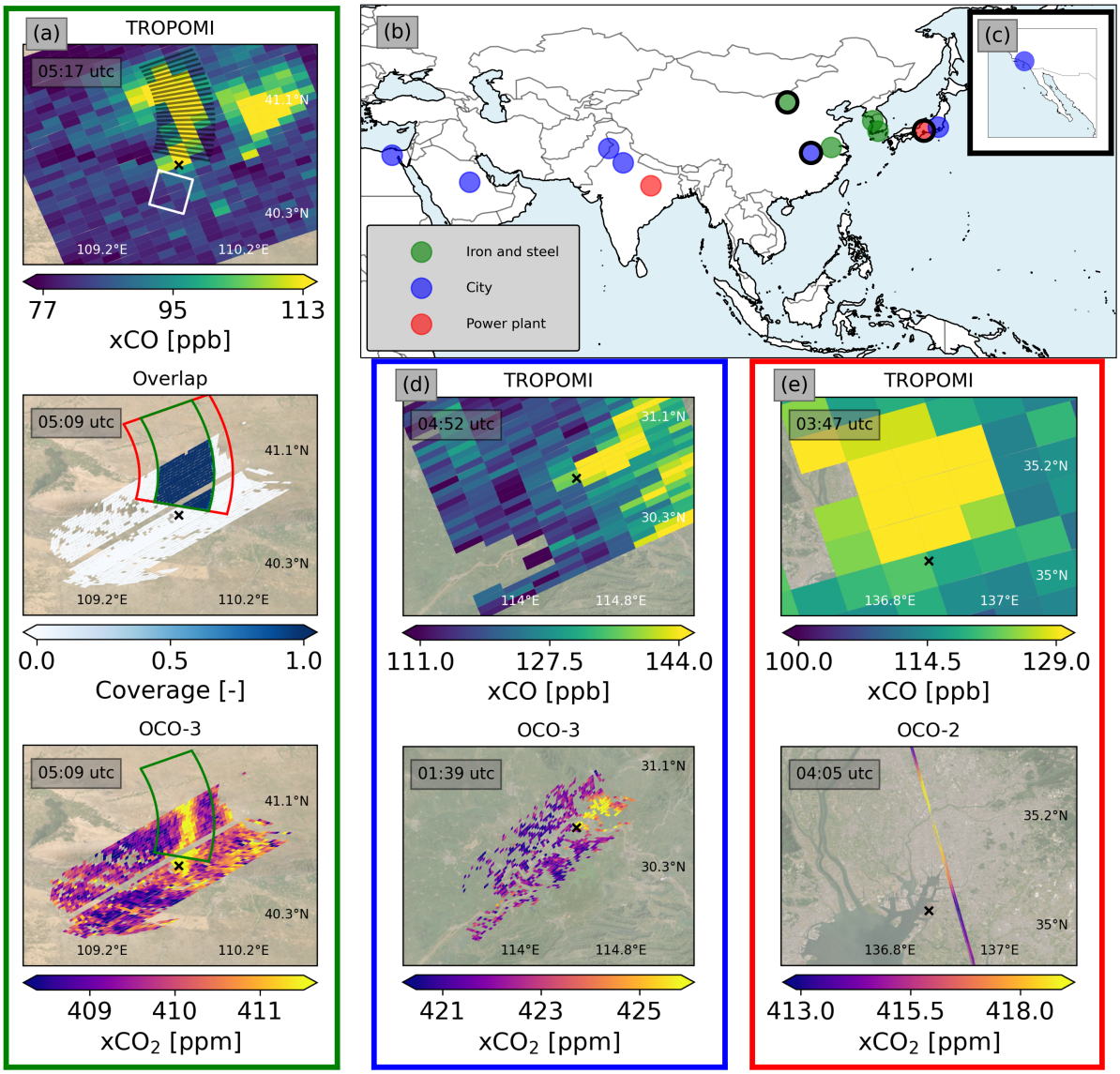

Figure 1: Locations of the sources investigated in this study are shown in panels (b) and (c), where the source type is indicated by different colors (blue: city; green: iron and steel plant; red: power plant). The latitude and longitude of the various sources are given in Appendix A. For each source type, panels (a), (d), and (e) show example TROPOMI CO and OCO CO_2 plumes observed on the same days for the sources located at the black-outlined markers in panel (b). Overpass times of the satellites are shown in UTC in the top left corners. Specifically, panel (a) shows TROPOMI and OCO-3 observations over the Baotou industrial complex on October 8, 2019; panel (d) shows Wuhan on June 9, 2023; and panel (e) shows observations over the Nippon power plant on May 11, 2019, with CO_2 data from OCO-2. Additionally, the upper figure in panel (a) shows the transects (black) and upwind background region (white) used in our method. Its middle figure shows in blue the region used to determine a CO to CO_2 enhancement ratio which we use to derive CO_2 emission rates. Highlighted in green we show the area spanned by the CSF transects, with the area used to calculate the background to the side of the plume shown in red. Background imagery comes from Esri, Maxar, Earthstar Geographics, and the GIS User Community (2022).

For observations covered by both TROPOMI and OCO-2, the assumption of similar transport holds due to the similarity of their orbits; the maximum difference in overpass time for observations used in this study is 37 minutes. However, the irregular orbits of OCO-3 can result in overpass time differences exceeding six hours, over which there can be considerable variation in transport conditions and emission strengths. As a balance between retaining sufficient OCO-3 observations and adhering to the assumption of similar transport, we only use days where the difference in observation time is less than four hours.

This way, the local overpass time of TROPOMI around 13:30 ensures all observations lie between 8 am and 6 pm local time. In addition, in Section 3.1, we use simulations to evaluate the effect of differences in overpass time.

2.4 Emission inventories

We compare our emission rates to the Emissions Database for Global Atmospheric Research (EDGAR) bottom-up emission inventory version 8 that provides emission rates up to 2022 (Crippa et al., 2024). As EDGAR provides both CO and CO_2 emission rates, we can compare the emission rates, as well as our observed enhancement ratios (e.g. combustion ratios). EDGAR achieves a spatial resolution of 0.1° globally by distributing national emission totals using spatial proxies. National activity data are converted into emission rates using emission factors following the IPCC methodology for greenhouse gases (Eggleston et al., 2006) and the EMEP/EEA emission inventory guidebook for air pollutants (Nielsen, 2013). We determine which pixels in EDGAR contribute to the source emissions in the same way as Leguijt et al. (2023); we sum emissions in the nine pixels closest to the source, and include any neighboring pixels with population densities (Gridded Population of the World (CIESIN (Center for International Earth Science Information Network), 2018)) exceeding the mean of its neighbors by one standard deviation. The EDGAR inventory is also used as input to the atmospheric modeling employed to test our methodology.

In addition to EDGAR, we compare our results to two CO_2-only bottom-up emission inventories. The Open-source Data Inventory for Anthropogenic CO_2 (ODIAC, Oda and Maksyutov (2011)) provides CO_2 emission rates for 2022 at 1x1 km^2 resolution, while Climate TRACE (Climate TRACE - Tracking Real-time Atmospheric Carbon Emissions, 2024) provides CO_2 emissions of point sources and transport. Finally, we compare to the point source emission database developed for the CO2MVS Research on Supplementary Observations (CORSO) project (`https://www.corso-project.eu`), which provides both CO and CO_2 emissions for 2021 (Guevara et al., 2024b). The CORSO point source database is an expanded version of the recently published global catalogue of CO_2 emissions and co-emitted species from power plants by Guevara et al. (2024a) which includes industrial facilities. Due to its focus on point sources, we are limited to a comparison for the non-urban sources.

2.5 WRF chemical transport model

We perform a model-based test of our approach using synthetic observations. For this, we use the Weather Research and Forecasting (WRF) chemical transport model version 4.1 (Powers et al., 2017) to simulate 3D concentration fields over the industrial complex of Baotou (China), and the cities of Delhi (India) and Wuhan (China). These sources show strong enhancements in the satellite data and relatively high number of OCO-observations.

As valid OCO-observations are sparse and distributed unevenly throughout the year, we select simulation windows with temporally dense CO_2 observations. For Baotou, we simulate concentration fields from January 2022 to June 2022, using January 2022 as spin-up month, for a total of thirteen OCO overpasses with downwind observations. For Delhi and Wuhan, we simulate September-December 2022 and September-October 2022, respectively, using September as spin-up in both. For both Delhi and Wuhan, this results in five days with same-day downwind observations from TROPOMI and OCO.

The simulations use double-nested domains centered at the source with a resolution of 3 km in the inner domain (147x147 km^2), 9 km in the middle domain (441x441 km^2), and 27 km in the outer domain (1323x1323 km^2). The nesting is required to use the CAMS global inversion-optimized greenhouse gas fluxes and concentrations v23r3 as CO_2 initial and 6-hourly boundary conditions which have a resolution of 1.4°x0.7° (Chevallier, 2023). As CO boundary conditions, we use the CAMS global air pollutant forecast at a resolution of 0.25°x0.25° (Inness et al., 2015). Transport is driven by meteorological fields from the National Centers for Environmental Prediction (NCEP, 2000). The simulations do not require chemistry due to the long lifetime of both species relative to the spatial domain of the simulations.

To represent the anthropogenic emissions within the domain, we use EDGAR v8 emissions. Sectoral emission rates are distributed along vertical profiles taken from Bieser et al. (2011). These vertical profiles parameterize the combination of injection height and plume rise for each emission sector. In addition, we use time profiles from Guevara et al. (2021) to simulate the temporal variation in each sector. For the Net Ecosystem Exchange (NEE), we use CO_2 data based on the vegetation-terrestrial ecosystem Lund-Potsdam-Jena General Ecosystem Simulator (LPJ-GUESS, Smith et al. (2014)), provided at a resolution of 0.5° by the Integrated Carbon Observation System (ICOS, Heiskanen et al. (2022)). We

use NEE emission rates at monthly resolution, averaging diurnal patterns over all days of the month.

To convert the simulated concentration fields to total columns as observed by the satellites, we sample the simulation output over each satellite's footprints at the hour closest to satellite overpass. Vertical sensitivity is taken into account by applying the averaging kernels (Landgraf et al., 2021; Taylor et al., 2023).

2.6 Uncertainty analysis

As our method is an extension of the CSF method described in Leguijt et al. (2023), we follow the same ensemble procedure to estimate uncertainties for our CO emission rate estimates. The ensemble is constructed by individually varying different parameters over appropriate ranges. For each location, we report the full spread of CO emission rate estimates in our ensemble as uncertainty. To quantify CO_2 emission rates, the CSF is followed by an enhancement ratio determination, leading to additional uncertainty in the final CO_2 emission rate estimates. This increased uncertainty is reflected in our uncertainty method by varying the region used for the background determination (upwind or next to the plume) and the maximum allowed overpass time difference for days to be included in the average.

The resulting contributions to the uncertainty of each ensemble member for both CO and CO_2 are shown in Appendix B. Appendix B also shows the ranges over which each parameter is varied.

3 Results and Discussion

In Section 3.1 we will first evaluate the performance of our method using simulated data, followed by a comparison to direct application of the CSF method on OCO-3 data. After these two evaluations based on simulations, we apply our method to observations at the thirteen considered sources to determine CO and CO_2 emission rates that we compare with bottom-up inventories and satellite-based findings in the literature in Sections 3.2 to 3.4.

3.1 Evaluation of the two-step methodology on simulated data

As a first step, we evaluate how well our approach performs on synthetic TROPOMI CO and OCO CO_2 observations. Based on visual inspection, we find that simulated plumes over Baotou and Delhi correspond well to observations both in location and order of magnitude (see Appendix C for Baotou). For Wuhan, we observe simulated CO enhancements exceeding 50 ppb (not shown here) which are not present to this degree in the TROPOMI observations. These enhancements originate from an oil refinery outside the city bounds present in EDGAR, which overshadows the simulated plume from Wuhan itself. Locations and emission rates of point sources like oil refineries have been found to be relatively uncertain (Kuenen et al., 2022). Based on these findings, and the absence of these high enhancements in the TROPOMI measurements, we remove the oil refinery's emissions from our simulations over Wuhan, which assures similarity between the simulations and observations. To ensure a realistic evaluation, we apply our two-step method using the NASA/GMAO GEOS-FP reanalysis data wind product (Molod et al., 2012), rather than the meteorological fields which drove the simulation (NCEP, 2000). Our mean CO emission rates for the three sources are within 13% of the simulation input (Appendix D), despite the low number of observation days in the simulated period (13 for Baotou and 5 for Delhi and Wuhan). The corresponding mean CO_2 emission rate estimates are within 31% of the simulation input and agree within uncertainty. For every source, the bias of the retrieved mean emission rate has the same direction for both CO and CO_2, but is larger in the CO_2 estimates.

To simulate realistic satellite observations, our simulations were sampled at the hour closest to the overpass time of the respective satellite. However, our simulations also allow the use of concentration fields at different hours. To investigate the effect of OCO-3's irregular observation times on our emission rate estimates, we sample the simulated CO_2 fields at hourly intervals for 24 hours on all 23 days with OCO observations. Because of its sun-synchronous orbit, and resulting stability in overpass times, we only use the CO simulations at the hour closest to the TROPOMI overpass. Hence, all 24 CO_2 emission rate estimates are using the same CO quantification. Variation in CO_2 emission rate estimates are driven by CO_2 plumes moving in and out of overlap with the CO plume, differences in wind speed, diurnal variation in CO_2 emission rates, and different transport conditions throughout the day. Overpass differences exceeding two hours result in lower mean emission quantifications (Appendix E). However, filtering of overpasses with time differences exceeding two hours would also remove up to 72% of the already sparse shared overpasses in our satellite observations. We find that the variability of individual

estimates of all considered sites (Section 3.2) is larger than the differences caused by differences in overpass analyzed here. As a result, our estimates are relatively insensitive to the time difference between observations. We therefore use a maximum allowed difference in overpass time of four hours. However, as the mean emission rates for the 23 investigated simulated plumes are low but stable over time differences exceeding four hours, we include all same-day estimates in our uncertainty ensembles (Appendix B).

We compare our TROPOMI/OCO-based CO_2 emission rates to a direct application of the CSF method on OCO observations. It is only possible to apply the CSF on high coverage observations, which means that we are limited to OCO-3's SAMs measurements. Similarly, the high natural CO_2 background requires that we only focus on very high-emission sources. The Baotou industrial complex in China satisfies both these requirements and is therefore selected for a comparison between both methods using simulated data. As the emission rate in a CSF method is proportional to the enhancement, Equation 3 shows the two methods are very similar if the same transects are used, and all transects are fully covered by observations. In practice, this is often not the case, and this is the reason why we developed the ratio enhancement approach which is less dependent on OCO's coverage. Figure 2 shows that five of the thirteen OCO-3 observations are not suited for emission quantification without the use of TROPOMI data due to a lack of coverage of the CO_2 plume in the OCO-3 observations (shown in gray). For most other days, we observe similar CO_2 emission rates whether we include TROPOMI data or not. We find consistent mean emission rates of 68.5 (41.1-95.9) Tg yr^{-1} using TROPOMI CO and 55.3 (31.6-79.0) Tg yr^{-1} using only OCO, compared to a simulation input of 63.0 Tg yr^{-1}. An example of a day where both methods result in similar emission rate estimates is shown in Figure 2b, where the downwind CO_2 coverage allows for complete transects, despite not having OCO measurements on the exact location of the industrial complex. However, Figure 2a also shows that a direct application of the CSF to OCO data results in a lower emission rate than our TROPOMI-based approach on most days. Panel (c) shows an example of such a day; as enhancements are integrated over transects, missing pixels in the plume result in incomplete integrals and underestimated emission rates. Therefore, days like this are not well suited for a direct CSF application and would not be usable without making assumptions on how to fill in the missing data. Using TROPOMI, the integrals over the transects are made using the complete coverage of TROPOMI, resulting in a higher, more complete, emission rate estimate. The OCO-observations are only used to determine a mean CO_2 enhancement, for which the coverage requirements are much lower and concern the total plume, rather than all transects individually. This example shows the strength of the combination of the two satellites.

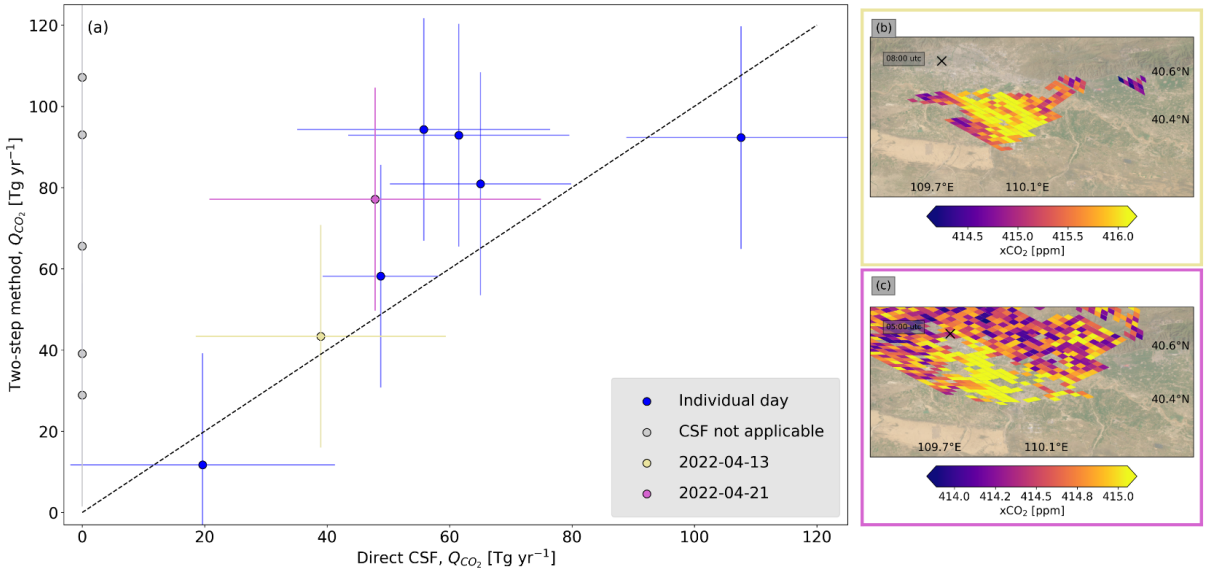

Figure 2: Comparison between CO_2 emission rate estimates using TROPOMI CO observations (y-axis) and CO_2 emission rate estimates from direct application of the CSF method to simulated OCO-3 data (x-axis). Gray dots represent days where the CSF could not be directly applied to the OCO-3 CO_2 data. The yellow dot corresponds to the plume over Baotou on the 13$^{\text{th}}$ of April 2022 shown in panel (b). Similarly, the magenta dot corresponds to panel (c), with a plume over Baotou on April 21, 2022. The black crosses indicate the center of the Baotou industrial complex. Uncertainties are indicated with the standard deviation of the emission estimates from the transects. Background imagery comes from Esri, Maxar, Earthstar Geographics, and the GIS User Community (2022).

3.2 Carbon monoxide emission estimates

Having applied our method to simulated data, we now apply it to six years of satellite observations over the thirteen investigated sources. We compare our TROPOMI-based Q_{CO} emission rates with those in the EDGAR inventory and the point source inventory developed in the CORSO project (Figure 3). Our emission estimates shown here only include days where we have observations from both TROPOMI and OCO as only those days can be used to later determine Q_{CO_2}. Appendix F covers a comparison to the full TROPOMI dataset, in which we show that the data used in Figure 3 are representative for the full TROPOMI data for all sources except for Cairo, Riyadh, and Baotou, which show slightly larger (15%, 21%, and 14%) emissions based on the full TROPOMI record.

Five of the seven investigated cities show significant differences between the TROPOMI and EDGAR emission estimates. The most sizeable differences are found for Lahore and Delhi that show lower CO emission rates based on TROPOMI, 278 (180-382) and 298 (268-375) Gg yr^{-1} respectively, compared to 408 and 621 Gg yr^{-1} in EDGAR. Our emission rate quantification for Los Angeles is significantly higher than EDGAR, but is more uncertain as the city is located in a basin where emitted CO can accumulate, thereby artificially increasing the emission estimates derived using the CSF method. Additionally, the accumulation in the basin makes it difficult to determine the spatial footprint of the underlying emissions. The EDGAR v8 CO emission rate estimate for Cairo lies much closer to our CSF estimate than the EDGAR v5 estimate previously studied in Leguijt et al. (2023). Previous approaches to quantify emissions of long-lived species have often relied on emission rates from inventories to convert enhancement ratios into emission rate estimates (Plant et al., 2022; Ohyama et al., 2024). Figure 3 shows that CO_2 estimates for five out of seven cities studied here would change less than 30% using CO estimates based on the satellite observations or the EDGAR database, even though our estimates only agree with EDGAR within uncertainty for two cities. Much larger differences are seen for the industrial sources, with four out of six showing substantially different TROPOMI-based CO emission rates compared to EDGAR. For all six industrial sources, our estimates are higher than reported in the CORSO inventory, although its emission estimate for the Hyundai Dangjin iron and steel plant aligns much better with our estimate than the EDGAR estimate. While Schneising et al. (2024) and Leguijt et al. (2025) showed comparable CO emission rates between facility-level reporting and satellite-based estimates for iron and steel plants in Europe, there appear to be much larger uncertainties in industrial emission estimates for

the iron and steel plants studied here.

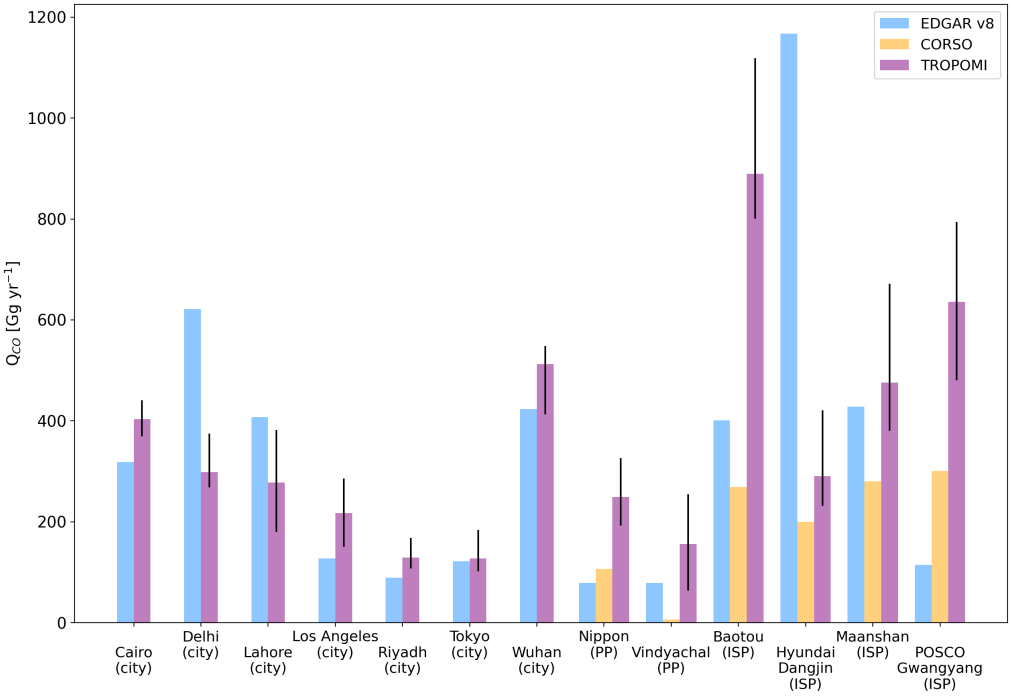

Figure 3: Comparison between CO emission rate estimates between our TROPOMI-based quantifications (purple), EDGAR v8 (blue), and CORSO (yellow) for the investigated cities, power plants (PP), and integrated iron and steel plants (ISP). Our estimates are based on data from 2018-2023, EDGAR (CORSO) emission rates are for 2022 (2021). The TROPOMI-based emission rate estimates only include days on which the CO_2 emission rate could also be estimated.

We further extend the comparison of our emission rate estimates to other work using OCO data (for CO_2 as covered in Sections 3.3 and 3.4) reported in the literature in Table 1. Our Q_{CO} city estimates for Tokyo and Delhi are lower than those determined by Ohyama et al. (2024), who calculate Q_{CO} by multiplying inventory CO_2 emissions by observed enhancement ratios. The difference between the EDGAR- and ODIAC-based Q_{CO} estimates for Delhi highlights the importance of independent verification of bottom-up emission estimates.

Location	Q_{CO} (Gg yr^{-1})	[CO]/[CO_2] (ppb ppm^{-1})	Q_{CO_2} (Tg yr^{-1})	Year	Source
Cairo	**403 (369-441)**	**25.3 (18.5-32.2)**	**30 (22-35)**	**'19-'23**	**This work**
$n_{ests} = 53$			38[a]	'14-'22	Wilmot et al. (2024)
			92 (84-100)	'14	Ye et al. (2020)
Delhi	**298 (269-375)**	**16.5 (6.4-29.9)**	**14 (7-23)**	**'19-'23**	**This work**
$n_{ests} = 24$	1400 (500-2300) (O)	20		'19-'23	Ohyama et al. (2024)
	500 (250-750) (E)			'19-'23	Ohyama et al. (2024)
			27[a]	'14-'22	Wilmot et al. (2024)
Lahore	**278 (180-382)**	**53.3 (20.1-133.2)**	**15 (4-32)**	**'19-'23**	**This work**
$n_{ests} = 11$			39 (21-58)	'19	Lei et al. (2021)
		1.4 (0.5-2.2)[b]		'18-'20	Park et al. (2021)
Los Angeles	**217 (150-286)**	**16.2 (6.6-23.0)**	**24 (9-46)**	**'19-'23**	**This work**
$n_{ests} = 92$		3.3 (2.7-3.8)[b]		'18-'20	Park et al. (2021)
		9.7 (9.2-10.2)		'20-'21	Wu et al. (2022)
			20[a]	'14-'22	Wilmot et al. (2024)
			280 (265-295)	'15	Ye et al. (2020)
Riyadh	**129 (107-168)**	**23.7 (12.6-38.1)**	**13 (2-30)**	**'19-'23**	**This work**
$n_{ests} = 48$			84 (14%)[c]	'15-'22	Jin et al. (2024)
			115 (94-137)	'14	Ye et al. (2020)
Tokyo	**128 (102-184)**	**5.6 (1.9-11.2)**	**41 (22-78)**	**'19-'23**	**This work**
$n_{ests} = 19$	650 (250-1050) (O)	5		'19-'23	Ohyama et al. (2024)
	775 (350-1200) (E)			'19-'23	Ohyama et al. (2024)
		4.1 (3.8-4.3)[b]		'18-'20	Park et al. (2021)
			57[a]	'14-'22	Wilmot et al. (2024)
Wuhan	**518 (418-554)**	**11.6 (8.9-20.3)**	**71 (50-103)**	**'19-'23**	**This work**
$n_{ests} = 13$			62[a]	'14-'22	Wilmot et al. (2024)
			199 (113-286)	'19	Zhang et al. (2023)
Baotou	**890 (801-1119)**	**25.9 (21.8-30.7)**	**94 (69-109)**	**'19-'23**	**This work**
$n_{ests} = 42$		17.3 (16.8-17.8)		'20-'21	Wu et al. (2022)

[a]Per capita emissions were converted to total emissions by summing the Gridded Population of the World (CIESIN (Center for International Earth Science Information Network), 2018).
[b]Conversion from mol m^{-2} to ppb was done by assuming standard pressure.
[c]This error is the mean relative error of the seven individual measurements.

Table 1: Comparison of our emission results to literature. n_{ests} equals the number of daily estimates used in our method. The footnotes denote assumptions made in the conversion of results to enable direct comparison. (O) and (E) refer to the inventory (ODIAC or EDGAR) that Ohyama et al. (2024) used for their Q_{CO} estimate.

3.3 Combustion efficiency estimates

Figure 4 shows a comparison between the observed CO/CO_2 enhancement ratios and EDGAR and CORSO emission ratios, where we take the molar-mass normalized emission ratios for the inventories. This ratio can be seen as an effective combustion efficiency. Similar to the CO results, we see large differences with EDGAR for Delhi, Lahore, and Los Angeles, 17 (6-30), 53 (19-133), and 16 (7-23) ppb ppm^{-1} compared to 68, 110, and 7 ppb ppm^{-1}. In EDGAR, Delhi and Lahore emit much higher quantities of CO per emitted CO_2 than the other cities, while in the TROPOMI data, we only see this for Lahore. Because both the observed enhancement ratio and the estimated CO emission rate are lower than in EDGAR for Delhi and Lahore, the CO_2 emission rates will show smaller differences than the individual components of their calculations. The accumulation of gas in the Los Angeles basin affects both CO and CO_2, and it therefore does not explain the lower combustion efficiency observed compared to the emission inventory. This difference might be a result of the extensive (difficult to estimate) spatial footprint of emission sources in Los Angeles. By far the largest difference in enhancement ratio is seen over Riyadh. While EDGAR and TROPOMI agreed within 44% on the CO emissions in Riyadh, there is a difference of 741% in enhancement ratio. The TROPOMI observed ratio for Riyadh of 24 (13-38) ppb ppm^{-1} is very similar to the ratio in Cairo (25 (19-32) ppb ppm^{-1}), while the EDGAR-based ratio is the lowest of all investigated cities. This high effective combustion efficiency in EDGAR is the result of large power plant emissions in Riyadh in the inventory. Additionally, the CO_2 enhancements seen in OCO are lower than expected based on the emission data in EDGAR.

As expected, observed CO over CO_2 ratios of power plants are much lower than those of the integrated iron and steel plants. The satellite-based enhancement ratios for three of the industrial complexes with iron and steel plants are much higher (on average 179%) than those in EDGAR. The same holds for all iron and steel plants in the CORSO inventory (on average 264%), while our combustion efficiency estimate is consistent with Wu et al. (2022) for Baotou (Table 1). The differences in enhancement ratios

suggest the discrepancy between TROPOMI and inventory industrial CO emissions in Figure 3 can be partly attributed to a potentially optimistic effective combustion efficiency, rather than uncertainties in the activity data of the plants. As an exception, our observed Q_{CO} and enhancement ratio for the Hyundai Dangjin iron and steel plant are much lower than predicted by EDGAR, with the observed enhancement ratio being closer to the values observed for the other iron and steel plants predicted by EDGAR.

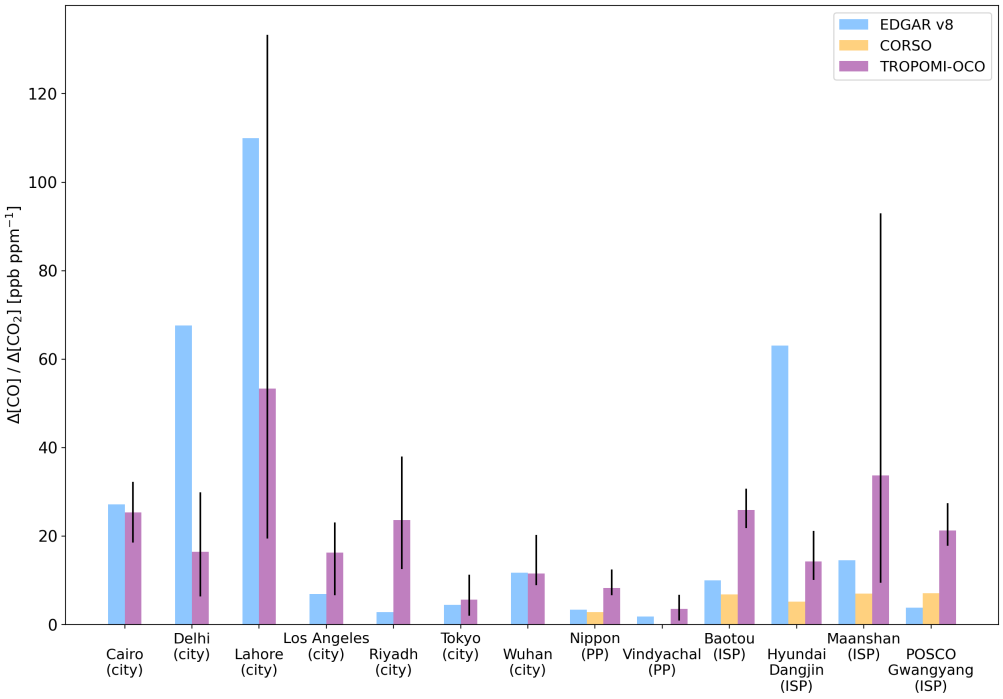

Figure 4: In purple, we show the mean enhancement ratio (CO/CO_2 in ppb ppm^{-1}) observed by TROPOMI and OCO, which can be used as a proxy for the effective combustion efficiency. In blue and yellow, we show the corresponding mass-normalized ratio of the emission rates from EDGAR version 8 and the CORSO inventory. As in Figure 3, the satellite data span 2018-2023 while the inventory values are for 2022 and 2021.

For the iron and steel plants studied here, no company reporting was available. For construction of the CORSO inventory, Guevara et al. (2024b) therefore relied on general emission ratios (e.g., from Hoesly et al. (2024)) to estimate CO emissions from CO_2 emissions and/or energy use. This is also reflected in the CORSO CO/CO_2 ratios for iron and steel plants that show a very limited range from 5 to 7 ppb ppm^{-1}, whereas our satellite-based ratios range between 14 and 34 ppb ppm^{-1}. Our enhancement ratios generally agree well with literature estimates from the GOSAT-based study by Ohyama et al. (2024) and the combination of TROPOMI with OCO-2 or OCO-3 by Park et al. (2021) and Wu et al. (2022) respectively. However, we observe an enhancement ratio in Lahore that exceeds the estimate by Park et al. (2021) by orders of magnitude. We do not have an explanation for this disparity, but, for this specific case, our estimate lies closer to the emission ratio given in EDGAR (Figure 4).

3.4 Carbon dioxide emission estimates

Combining our TROPOMI-based CO emission rate estimates with the observed enhancement ratios, we calculate CO_2 emission rates. Figure 5 shows the resulting Q_{CO_2} estimates and inventory estimates from EDGAR, ODIAC, Climate TRACE, and CORSO obtained by summing emissions over the same area used for the EDGAR CO estimates. Despite the low number of OCO-2 and OCO-3 observations, our estimates show good agreement with EDGAR for the two power plants, Los Angeles, and Tokyo, for which the CO_2 emissions should be relatively well known. There are, however, large differences between

our estimates, EDGAR and at least one of the other inventories for these four locations. As expected from the CO and CO/CO_2 results, the satellite-based CO_2 emission estimates are higher than EDGAR for Delhi and Lahore (38 (19-61) and 15 (4-32) Tg yr^{-1} compared to 14 and 6 Tg yr^{-1}). For these two cities, we find better agreement between our estimates and ODIAC, while EDGAR and Climate TRACE are similar. ODIAC is also closer to our emission estimate for Cairo while both EDGAR and Climate TRACE suggest lower CO_2 emission rates. The closer agreement between our estimates and ODIAC could suggest a potential underestimation of activity data in these cities in the EDGAR inventory. The previously observed difference in enhancement ratio for Riyadh results in a CO_2 emission rate estimate that is 74 (39-96)% lower than EDGAR. While our TROPOMI estimate (13 (2-30) Tg yr^{-1}) agrees well with Climate TRACE (15 Tg yr^{-1}), both EDGAR and ODIAC suggest higher emission rates. The EDGAR CO_2 emission estimate for Riyadh is largely driven by power plant emissions. However, the absence of domestic emissions in Climate TRACE could play a role in explaining the lower Climate TRACE estimates (both for Riyadh and Tokyo), despite the close agreement with EDGAR for most locations.

The CO_2 emission rates of iron and steel plants show much better agreement with EDGAR than their CO emissions, although both Maanshan and Baotou still show significant differences (94 (69-109) and 20 (15-33) Tg yr^{-1} compared to 63 and 46 Tg yr^{-1}). The better agreement between EDGAR and our CO_2 estimates suggests that differences in CO emission rates are driven by potential overestimation of the effective combustion efficiency for these industrial complexes, rather than mismatches in their activity data. There remains a relatively large spread between the iron and steel CO_2 emission estimates from different inventories. Noticeably, the Hyundai Dangjin plant has close to zero emissions in the ODIAC database, while the CORSO inventory estimates the highest inventory CO_2 emissions for all four plants. However, none of the four inventories shows significantly better agreement to our estimates than the others with R^2-values ranging from 0.07 to 0.41.

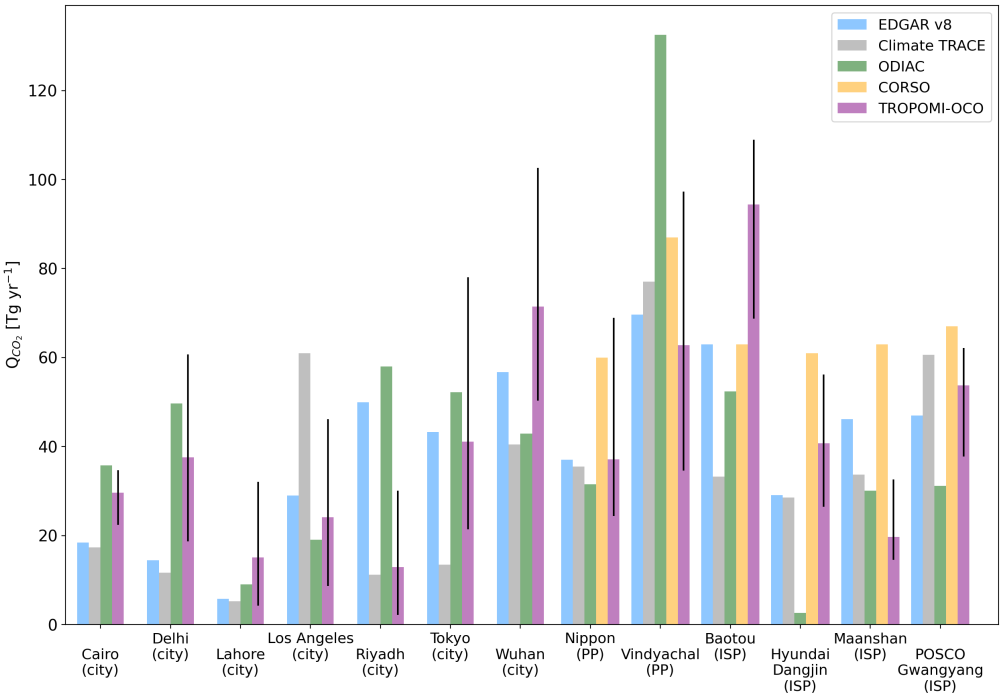

Figure 5: Comparison between our satellite-based CO_2 emission estimates (purple) for 2018-2023 to EDGAR v8 (blue, 2022), Climate TRACE (gray, 2022), ODIAC (green, 2022), and CORSO (yellow, 2021).

Our Q_{CO_2} estimates generally show good agreement to Wilmot et al. (2024), who calculate per capita CO_2 emissions from enhanced OCO-2 measurements over simulated spatial footprints. The differences in Q_{CO_2} are likely the result of the conversion from per capita emissions to city-wide totals. Our CO_2

emission estimate for Riyadh is much lower than those estimated from regional inversions performed with OCO-2 by Jin et al. (2024) and Ye et al. (2020), which could partly be attributed to the different spatial scales considered. However, combined with the higher CO_2 emissions in EDGAR and ODIAC, this suggests we may underestimate Q_{CO_2} for Riyadh. Similarly, our estimate for Los Angeles is also an order of magnitude lower than the Ye et al. (2020) estimate. However, like for Riyadh, Ye et al. (2020) estimate emissions for much larger domains than are considered in this paper, and their emission estimate encompasses the entire Los Angeles basin.

4 Conclusions

We have combined CO satellite measurements from TROPOMI with CO_2 data from the OCO instruments to provide CO and CO_2 emission rate estimates for seven cities and six industrial complexes that are independent of atmospheric modeling or prior bottom-up information. The emission rates are based on an extension of the Cross-Sectional Flux (CSF) method, which levies the high spatial coverage of TROPOMI to estimate CO emissions, and estimates CO_2 emissions by using the ratio between near-concurrent TROPOMI CO and OCO-2/3 CO_2 observations.

We tested our approach on synthetic data for three locations, finding CO (CO_2) emission estimates within 13% (31%) of the input emissions. We also showed that larger differences between the observation times of both satellites resulted in underestimated emissions. However, such an effect was not seen in emission quantifications of observed plumes due to the high variability of individual estimates. When compared to a CSF directly applied to OCO-3 data, we found similar emission rates on days where a direct CSF was possible. However, the use of TROPOMI CO data allowed for successful CO_2 emission estimates on many more days.

Applying our approach to the satellite observations, we found that our CO emission estimates are higher than the EDGAR emission inventory for all sources except for Delhi, Lahore, and the Hyundai Dangjin industrial complex. For five out of seven investigated cities, we found agreement with EDGAR within 30%. We only found this agreement for one of the four investigated iron and steel plants, with our CO emission estimates differing from EDGAR by more than 100% for the remaining three plants. Similarly, our CO emission estimates exceeded estimates from the CORSO inventory for all industrial sources. This comparison showed that the use of inventory CO estimates could bias ratio-based methods that rely on inventory data.

This disparity in CO emission rates was also reflected in the observed enhancement ratios, which showed differences with the molar-mass normalized inventory emission ratios exceeding 100% for the same three iron and steel plants. We also found a much larger variability of the enhancement ratio between facilities than present in the CORSO inventory. The observed enhancement ratios of Delhi and Lahore were lower than those in EDGAR, suggesting higher than expected combustion efficiencies.

Despite the temporal sparsity of CO_2 observations, we showed that our CO_2 emission estimates are consistent with those given in EDGAR for eight out of thirteen locations. We found large differences between the different inventories, with at least one outlying estimate for most of the sources, exemplifying the need for independent verification of emission rate estimates. Differences between our estimates and the EDGAR emission inventory indicated a potential overestimation of the effective combustion efficiency for the investigated integrated iron and steel complexes. In addition, our emission estimates indicated higher emission rates for Cairo, Delhi, and Lahore. A comparison to the ODIAC inventory indicated this difference might be due to a potential underestimation of activity data in these cities in the EDGAR inventory. Comparing our results with literature, we generally found good agreement where a direct comparison could be made. However, specifically for Riyadh, large scale atmospheric inversions seemed to indicate that our emission estimate is too low.

While our method could be extended to other large cities, specifically those with targeted OCO-3 observations, the number of CO-intense industries with targeted OCO observations is limited. The launch of the CO2M satellite instruments (Sierk et al., 2019) will significantly increase CO_2 coverage and provide concurrent NO_2 observations. As CO2M does not provide CO observations, our work shows how TROPOMI - and subsequently also Sentinel-5 - observations could be used in combination with CO2M to determine combustion efficiencies. The similarity in the orbit of Sentinel-5 and CO2M would also significantly increase the number of observations with overpass differences under 2 hours, for which our approach is best suited. The combination of CO_2 with both NO_2 and CO can help to disentangle sectoral contributions to emission plumes, which can provide independent space-based verification of emission rates and improve our understanding of emissions.

Author contributions

GL and JDM designed the study. GL performed the TROPOMI analysis with contributions from all authors. GL, IA, and JDM contributed to the initial draft of the paper. HN provided support for the interpretation of the OCO carbon dioxide data. GL wrote the paper with contributions from all authors.

Data availability

TROPOMI CO data (https://doi.org/10.5270/S5P-bj3nry0, Copernicus Sentinel- 5P, 2021) are publicly available at https://dataspace.copernicus.eu (last access: 2 April 2024). OCO-2 and OCO-3 CO_2 data are publicly available at https://disc.gsfc.nasa.gov/datasets (last access: 7 January 2025). GEOS-FP wind data are available via https://gmao.gsfc.nasa.gov/GMAO_products (Molod et al., 2012) (last access: 5 January 2024). WRF-Chem code is available at https://github.com/wrf-model/WRF/releases (Powers et al., 2017); in this work, version 4.1.5 was used (last access: 2 April 2024). Net ecosystem exchange CO_2 emissions from the LPJ-GUESS model are publicly available at https://www.icos-cp.eu/data-products/global-hourly-nee-gpp-and-total-respiration-2010-2022-based-lpj-guess-generated-2023 (Smith et al., 2014) (last access: 30 July 2024). EDGAR v8 CO and CO_2 emission grids are freely available at https://edgar.jrc.ec.europa.eu/emissions_data_and_maps (last access: 14 August 2024). The ODIAC CO_2 emission grid is freely available at https://db.cger.nies.go.jp/dataset/ODIAC/DL_odiac2023.html (Oda and Maksyutov, 2011) (last access: 5 December 2024). CO_2 emissions from Climate TRACE are freely available at https://climatetrace.org/data (Climate TRACE - Tracking Real-time Atmospheric Carbon Emissions, 2024) (last access: 29 May 2024). The CO and CO_2 point-source emissions used in this work developed in the CORSO project (Guevara et al., 2024b) are available upon request (contact: Hugo Denier van der Gon, hugo.deniervandergon@tno.nl), and will be available from https://www.corso-project.eu/ in due time.

Acknowledgements

We thank the team that realized the TROPOMI instrument and its data products, consisting of the partnership between Airbus Defence and Space Netherlands, KNMI, SRON and TNO, commissioned by NSO and ESA. Sentinel-5 Precursor is part of the EU Copernicus program, and Copernicus Sentinel-5P data (2018-2023) have been used. We also thank the teams that realized the OCO instruments, from which we used 2018-2023 data. These data were produced by the OCO-2 and OCO-3 projects at the Jet Propulsion Laboratory, California Institute of Technology, and obtained from the OCO-2 and OCO-3 data archives maintained at the NASA Goddard Earth Science Data and Information Services Center. Part of this work was carried out on the Dutch national e-infrastructure, and we thank SURF (www.surf.nl) for the support in using the National Supercomputer Snellius. The presented work was partly funded through the CORSO project which received funding from European Union's Horizon 2020 Research and Innovation Programme under grant agreement No101082914. This work was funded in part by an appointment to the NASA Postdoctoral Program at the Jet Propulsion Laboratory, California Institute of Technology, administered by Oak Ridge Associated Universities under contract with NASA.

Appendix A Source locations

Name	Country	Source type	Latitude, longitude
Baotou	China	Iron and steel, power plant	(40.648,109.7409)
Maanshan	China	Iron and steel	(31.6989,118.4682)
Wuhan	China	City	(30.62,114.45)
Cairo	Egypt	City	(30.15,31.3)
Delhi	India	City	(28.65,77.17)
Vindyachal	India	Power plant	(24.0983,82.6719)
Nippon	Japan	Iron and steel	(35.0276,136.8706)
Tokyo	Japan	City	(35.72,139.72)
Lahore	Pakistan	City	(31.5,74.3)
Riyadh	Saudi Arabia	City	(24.8,46.7)
Hyundai Dangjin	South Korea	Iron and steel	(36.9863,126.6974)
POSCO Gwangyang	South Korea	Iron and steel	(34.9201,127.7487)
Los Angeles	United States	City	(34.00,-118.28)

Table 2: Location of the sources studied in this work.

Appendix B Uncertainty ensemble

Figure 6 shows the uncertainty in our CO and CO_2 emission estimates for the different ensemble members. These uncertainties were obtained by varying the emission quantification parameters over the ranges given in Table 3 for all locations. The CO_2 ensembles also include different methods to determine the background, and different maximum allowed time differences for each of the ensemble members.

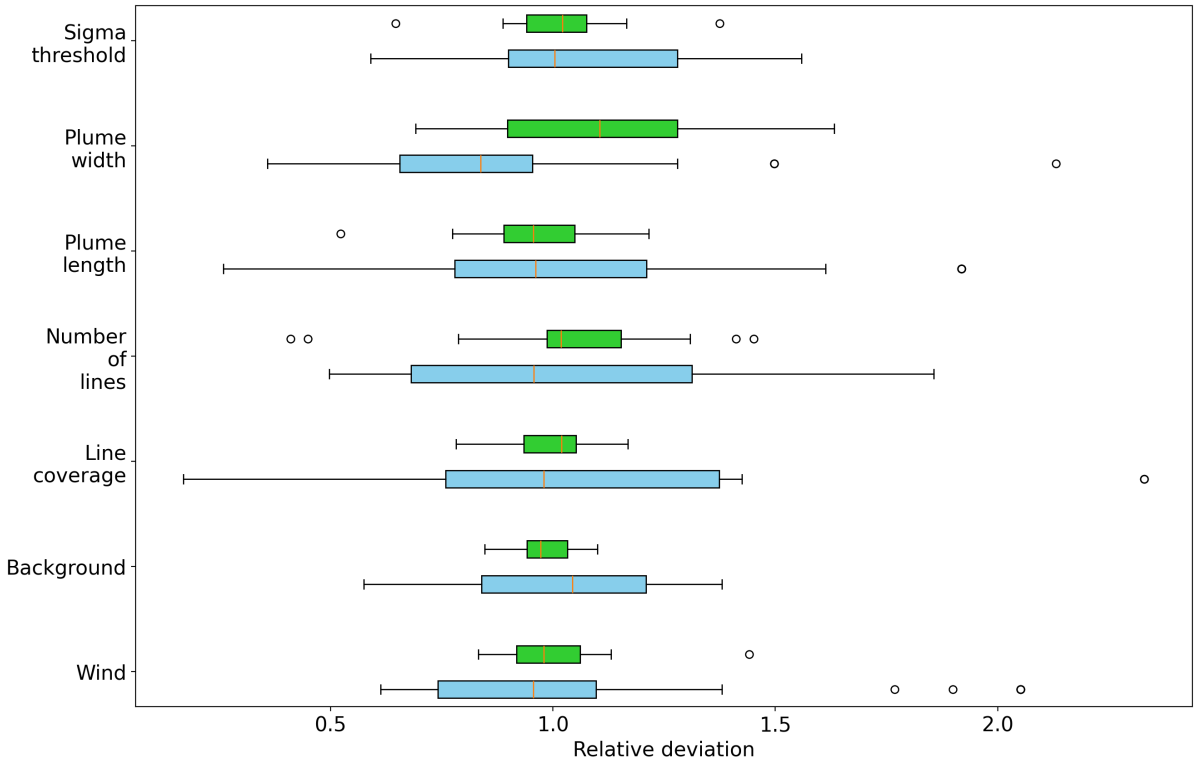

Figure 6: Spread in the uncertainty ensemble broken down per parameter. Green boxes correspond to CO uncertainties, while the CO_2 uncertainties are shown in blue.

Table 3: Variables used in the uncertainty analysis and the ranges over which they were varied. The resulting ensemble spreads are reported as uncertainty.

Parameter	**Range**	**Default**
Wind database	GEOS-fp 10m, ERA5 10m	GEOS-fp 10m
Standard deviation threshold for spline pixels	{1.2 - 2.4}	1.8
Number of transects	{10 - 40}	25
Minimum pixel coverage per transect	{50% - 90%}	70%
Distance of background box	{0.1° - 0.3°}	0.2°
Plume length	{0.6° - 1.0°}	0.8°
Transect width	{0.2° - 0.4°}	0.3°
Maximum overpass time difference (CO_2 only)	4 hours, 6 hours, same day	4 hours
Background region (CO_2 only)	upwind, next to transects	upwind

Appendix C Comparison between simulation and observation

Figure 7 shows simulated CO and CO_2 enhancements for Baotou on April 21, 2022, as well as the corresponding satellite observations. The CO simulations compare well with the observations, with the difference in enhancement strength indicating that the EDGAR emissions used as input to the simulation are lower than those observed by TROPOMI. Similarly, the observed CO_2 enhancements are higher than those simulated with WRF. The simulated CO_2 background concentrations (not shown here) are lower than those observed by OCO-3, indicating underestimated boundary conditions. Observed differences are generally in the order of 2 to 3 ppm. As our quantification method subtracts the background concentrations, this difference should not affect our emission estimates.

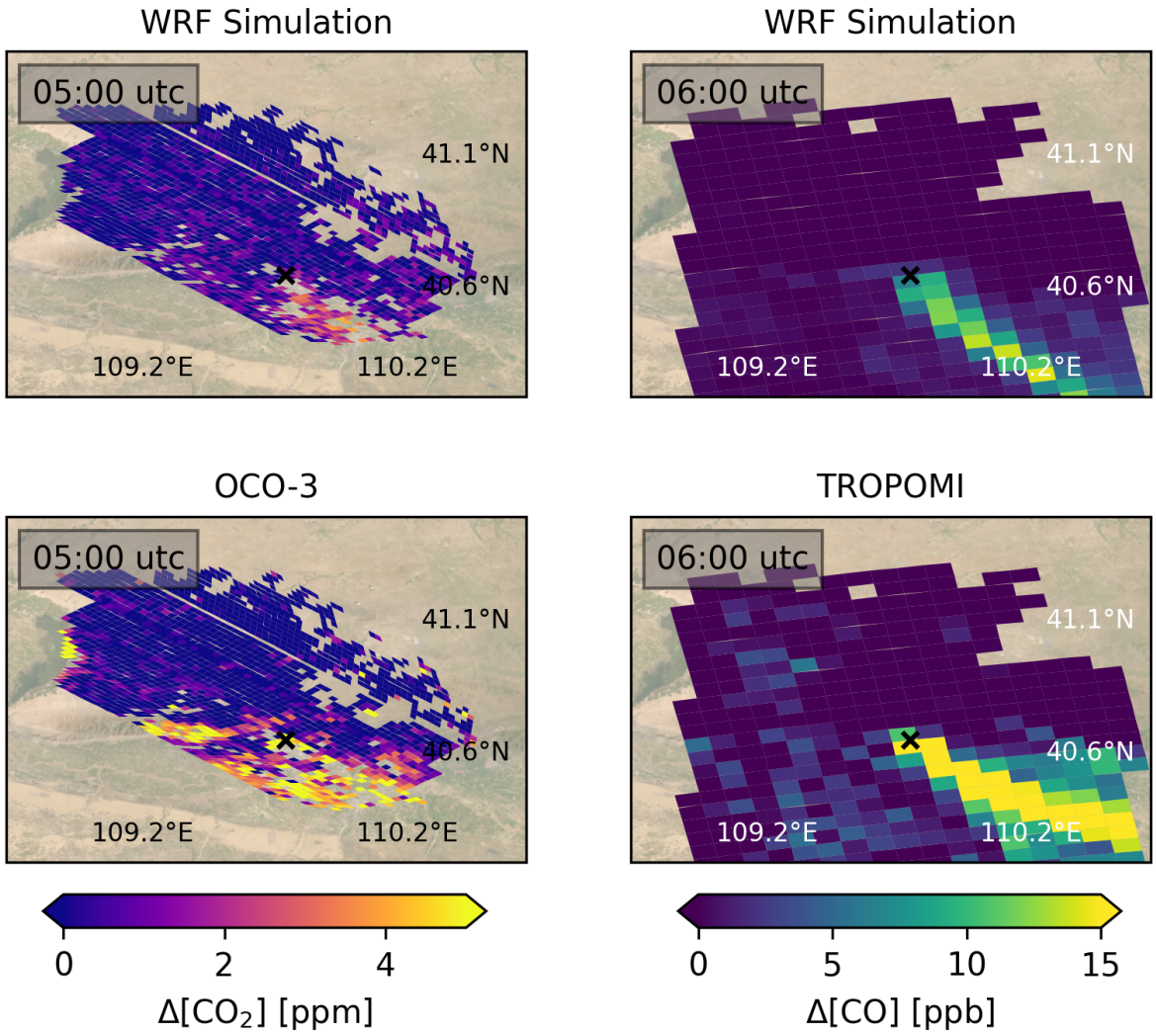

Figure 7: The top panels show simulated CO_2 and CO enhancement fields for Baotou on April 21, 2022 sampled as OCO and TROPOMI would observe the area. Lower panels show the corresponding OCO-3 and TROPOMI observations. Median concentrations have been subtracted to facilitate comparison of the enhanced regions. The black crosses indicate the center of the Baotou industrial complex. Background imagery comes from Esri, Maxar, Earthstar Geographics, and the GIS User Community (2022).

Appendix D Two-step method performance on simulated data

We evaluate the performance of our two-step method by applying it to simulated data. Figure 8 shows how well we are able to quantify the CO and CO_2 emission rates of the three simulated sources. All estimated emission rates agree with the simulation input within uncertainty. However, the mean CO emission estimates are closer to the simulated truth than the CO_2 results, which reflects the added uncertainty of combining data from multiple satellites.

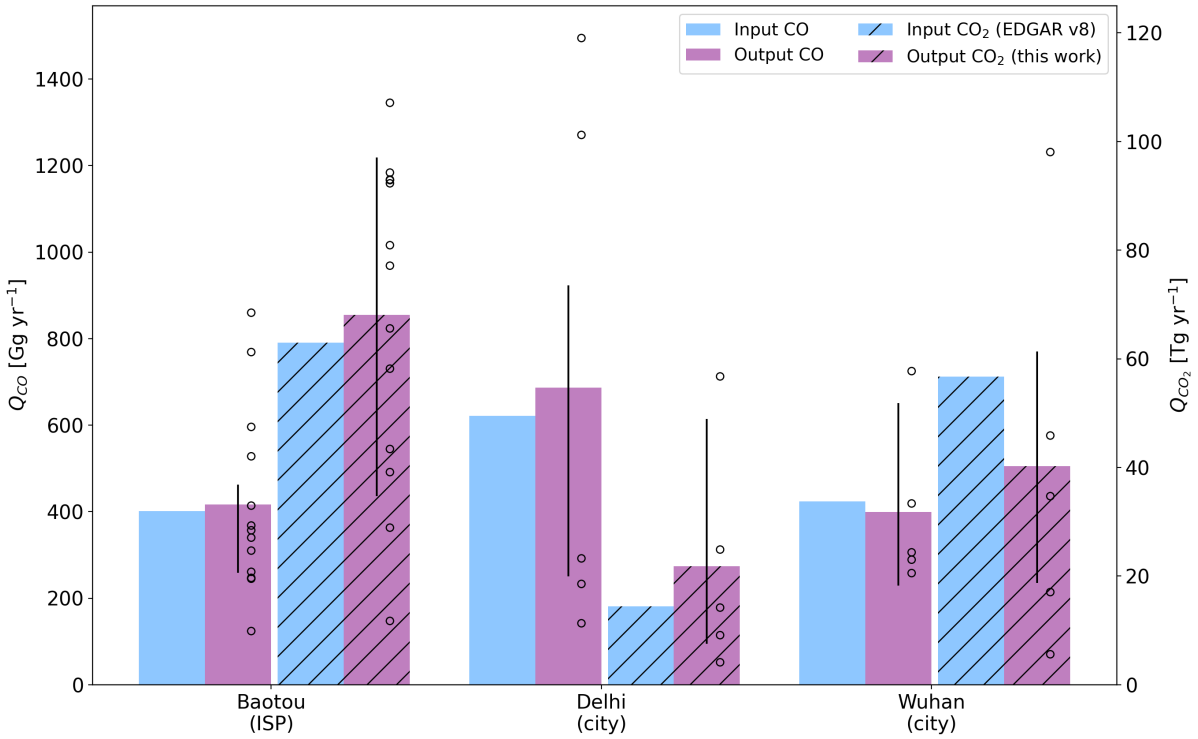

Figure 8: CO (left y-axis) and CO_2 (hashed, right y-axis) emission rates retrieved from applying our method to synthetic data simulated with WRF. The emission rates from EDGAR version 8, used as input to our simulations, are shown in blue, while the mean retrieved emission rate is shown in purple. The indicated uncertainty denotes the full spread of the uncertainty ensembles. Individual quantifications are shown as black circles.

Appendix E Differences in overpass-time

We use the synthetic data to evaluate how our method is affected by the variable overpass time of OCO-3. Figure 9 shows how the assumption of similar transport breaks down with increasing difference in overpass time of the two satellites. For the simulated plumes considered, differences in overpass time exceeding two hours result in significant underestimations of emission strengths.

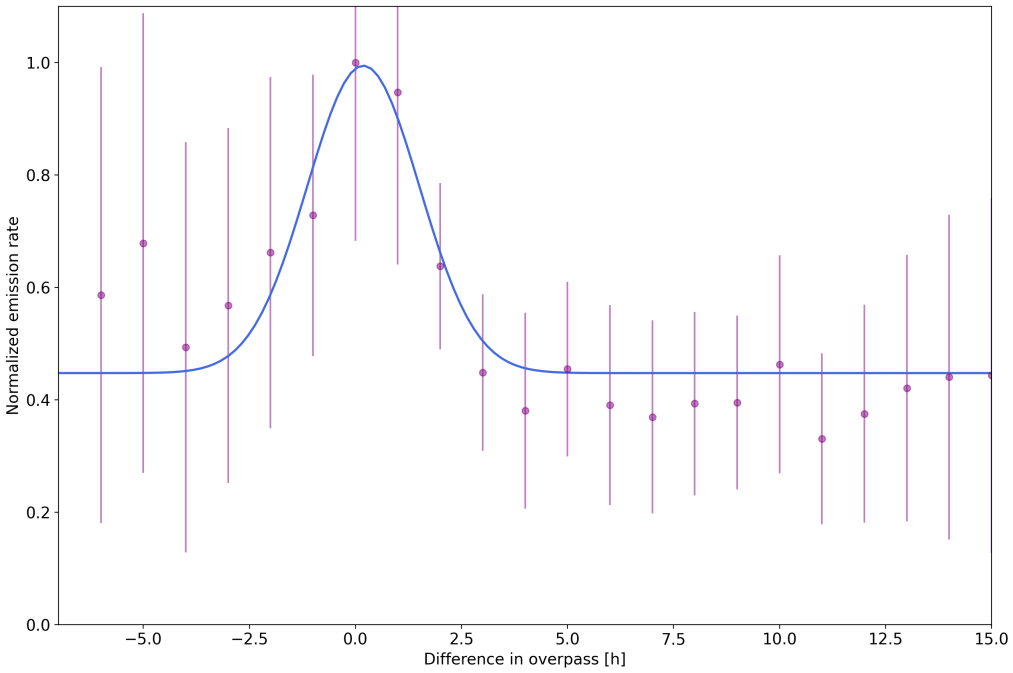

Figure 9: Variation in emission rate estimates due to the breaking down of the assumption of identical transport of the observed CO_2 and CO plumes. CO_2 emission rates, shown as purple dots, are normalized to the maximum estimated emission rate on each day. Each dot represents the average emission rate over the 23 simulated days with shared satellite observations while the error bars represent the standard deviation of the emission estimates. In blue, we show a Gaussian distribution with offset, fitted to the data using a non-linear least squares regression.

Appendix F Extension to full TROPOMI coverage

As mentioned in Section 2, we only apply our method to days with coverage in both TROPOMI and OCO-2 or OCO-3. Due to the difference in coverage of the satellites, this means a lot of TROPOMI observations are not used. To verify whether the subset of TROPOMI observations is representative for the total number of overpasses, we compare the different emission estimates in Figure 3 to those based on the full TROPOMI coverage for 2018-2023. As shown in Figure 10, we find that the limited and full coverage estimates are consistent in terms of being smaller or larger than EDGAR v8. We find that using only days with observations in both satellites results in CO emission rate estimates that are biased low for Cairo, Riyadh, and Baotou.

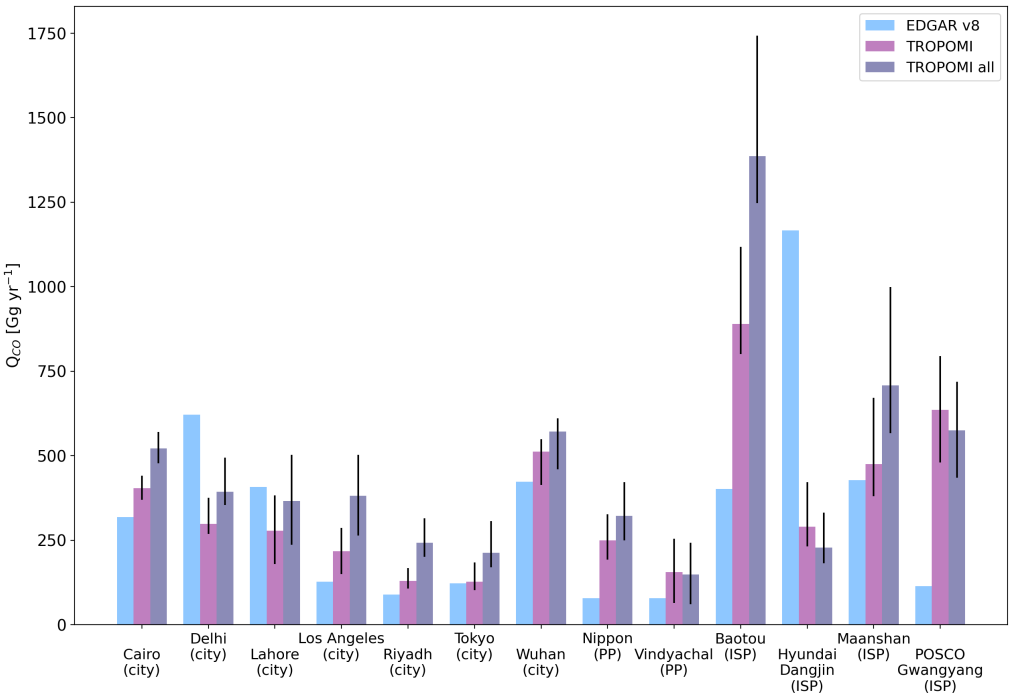

Figure 10: Comparison between EDGAR version 8 and our Q_{CO} estimates, similar to Figure 3. Additionally, we show a comparison to CO emission rate estimates derived using the full TROPOMI dataset from 2018-2023 (dark purple bar).

References

Bieser, J., Aulinger, A., Matthias, V., Quante, M., Van Der Gon, H.D., 2011. Vertical emission profiles for europe based on plume rise calculations. Environmental Pollution 159, 2935–2946. doi:https://doi.org/10.1016/j.envpol.2011.04.030.

Borsdorff, T., Aan de Brugh, J., Hu, H., Aben, I., Hasekamp, O., Landgraf, J., 2018. Measuring carbon monoxide with tropomi: First results and a comparison with ecmwf-ifs analysis data. Geophysical Research Letters 45, 2826–2832. doi:https://doi.org/10.1002/2018GL077045.

Chatterjee, A., Payne, V., Eldering, A., Rosenberg, R., Kiel, M., Fisher, B., Nelson, R., Dang, L., Rodrigues, G., O'Dell, C., et al., 2022. Orbiting carbon observatory-3 (oco-3) data quality statement: Level 2 forward and retrospective processing data release 10.4. https://docserver.gesdisc.eosdis.nasa.gov/public/project/OCO/OCO3_L2_DQ_Statement_v10_v104.pdf. [Last access Jan. 31, 2025].

Chen, Z., Jacob, D.J., Nesser, H., Sulprizio, M.P., Lorente, A., Varon, D.J., Lu, X., Shen, L., Qu, Z., Penn, E., et al., 2022. Methane emissions from china: a high-resolution inversion of tropomi satellite observations. Atmospheric Chemistry and Physics 22, 10809–10826. doi:https://doi.org/10.5194/acp-22-10809-2022.

Chevallier, F., 2023. Cams global inversion-optimised greenhouse gas fluxes and concentrations. https://ads.atmosphere.copernicus.eu/datasets/cams-global-greenhouse-gas-inversion. Accessed: 2024-12-21.

CIESIN (Center for International Earth Science Information Network), 2018. Gridded population of the world, version 4 (gpwv4): Population density, revision 11. doi:https://doi.org/10.7927/H49C6VHW. accessed: 2025-01-07.

Climate TRACE - Tracking Real-time Atmospheric Carbon Emissions, 2024. Climate TRACE Emissions Inventory. https://climatetrace.org.

Crippa, M., Guizzardi, D., Pagani, F., Schiavina, M., Melchiorri, M., Pisoni, E., Graziosi, F., Muntean, M., Maes, J., Dijkstra, L., et al., 2024. Insights into the spatial distribution of global, national, and subnational greenhouse gas emissions in the emissions database for global atmospheric research (edgar v8. 0). Earth System Science Data 16, 2811–2830. doi:https://doi.org/10.5194/essd-16-2811-2024.

Eggleston, H., Buendia, L., Miwa, K., Ngara, T., Tanabe, K., 2006. 2006 ipcc guidelines for national greenhouse gas inventories .

Eldering, A., Taylor, T.E., O'Dell, C.W., Pavlick, R., 2019. The oco-3 mission: measurement objectives and expected performance based on 1 year of simulated data. Atmospheric Measurement Techniques 12, 2341–2370. doi:https://doi.org/10.5194/amt-12-2341-2019.

Eldering, A., Wennberg, P., Crisp, D., Schimel, D., Gunson, M., Chatterjee, A., Liu, J., Schwandner, F., Sun, Y., O'dell, C., et al., 2017. The orbiting carbon observatory-2 early science investigations of regional carbon dioxide fluxes. Science 358, eaam5745. doi:10.1126/science.aam5745.

Esri, Maxar, Earthstar Geographics, and the GIS User Community, 2022. World imagery. https://services.arcgisonline.com/ArcGIS/rest/services/World_Imagery/MapServer. Accessed: 2025-01-07.

Fuentes Andrade, B., Buchwitz, M., Reuter, M., Bovensmann, H., Richter, A., Boesch, H., Burrows, J.P., 2024. A method for estimating localized co 2 emissions from co-located satellite xco 2 and no 2 images. Atmospheric Measurement Techniques 17, 1145–1173. doi:https://doi.org/10.5194/amt-17-1145-2024.

Green, R.O., Mahowald, N., Thompson, D.R., Ung, C., Brodrick, P., Pollock, R., Bennett, M., Lundeen, S., Joyce, M., Olson-Duvall, W., et al., 2023. Performance and early results from the earth surface mineral dust source investigation (emit) imaging spectroscopy mission, in: 2023 IEEE aerospace conference, IEEE. pp. 1–10. doi:10.1109/AERO55745.2023.10115851.

Guevara, M., Enciso, S., Tena, C., Jorba, O., Dellaert, S., Denier van der Gon, H., Pérez García-Pando, C., 2024a. A global catalogue of co2 emissions and co-emitted species from power plants, including high-resolution vertical and temporal profiles. Earth System Science Data 16, 337–373. doi:https://doi.org/10.5194/essd-16-337-2024.

Guevara, M., Jorba, O., Tena, C., Denier van der Gon, H., Kuenen, J., Elguindi, N., Darras, S., Granier, C., Pérez García-Pando, C., 2021. Copernicus atmosphere monitoring service temporal profiles (cams-tempo): global and european emission temporal profile maps for atmospheric chemistry modelling. Earth System Science Data 13, 367–404. doi:https://doi.org/10.5194/essd-13-367-2021.

Guevara, M., Val, A., Collado, O., Dellaert, S., Denier van der Gon, H., 2024b. Corso deliverable d1.2 improved global point source emissions dataset. https://www.corso-project.eu.

Guo, W., Shi, Y., Liu, Y., Su, M., 2023. Co2 emissions retrieval from coal-fired power plants based on oco-2/3 satellite observations and a gaussian plume model. Journal of Cleaner Production 397, 136525. doi:https://doi.org/10.1016/j.jclepro.2023.136525.

Hakkarainen, J., Szeląg, M.E., Ialongo, I., Retscher, C., Oda, T., Crisp, D., 2021. Analyzing nitrogen oxides to carbon dioxide emission ratios from space: A case study of matimba power station in south africa. Atmospheric Environment: X 10, 100110. doi:https://doi.org/10.1016/j.aeaoa.2021.100110.

Heiskanen, J., Brümmer, C., Buchmann, N., Calfapietra, C., Chen, H., Gielen, B., Gkritzalis, T., Hammer, S., Hartman, S., Herbst, M., et al., 2022. The integrated carbon observation system in europe. Bulletin of the American Meteorological Society 103, E855–E872. doi:https://doi.org/10.1175/BAMS-D-19-0364.1.

Hoesly, R., Smith, S.J., Prime, N., Ahsan, H., Suchyta, H., O'Rourke, P., Crippa, M., Klimont, Z., Guizzardi, D., Behrendt, J., Feng, L., Harkins, C., McDonald, B., Mott, A., McDuffie, A., Nicholson, M., Wang, S., 2024. Ceds v_2024_07_08 release emission data (v_2024_07_08). doi:https://doi.org/10.5281/zenodo.12803197.

Horowitz, C.A., 2016. Paris agreement. International Legal Materials 55, 740–755. doi:https://doi.org/10.1017/S0020782900004253.

Houweling, S., Baker, D., Basu, S., Boesch, H., Butz, A., Chevallier, F., Deng, F., Dlugokencky, E., Feng, L., Ganshin, A., et al., 2015. An intercomparison of inverse models for estimating sources and sinks of co2 using gosat measurements. Journal of Geophysical Research: Atmospheres 120, 5253–5266. doi:https://doi.org/10.1002/2014JD022962.

Imasu, R., Matsunaga, T., Nakajima, M., Yoshida, Y., Shiomi, K., Morino, I., Saitoh, N., Niwa, Y., Someya, Y., Oishi, Y., et al., 2023. Greenhouse gases observing satellite 2 (gosat-2): mission overview. Progress in Earth and Planetary Science 10, 33. doi:https://doi.org/10.1186/s40645-023-00562-2.

Inness, A., Blechschmidt, A.M., Bouarar, I., Chabrillat, S., Crepulja, M., Engelen, R., Eskes, H., Flemming, J., Gaudel, A., Hendrick, F., et al., 2015. Data assimilation of satellite-retrieved ozone, carbon monoxide and nitrogen dioxide with ecmwf's composition-ifs. Atmospheric chemistry and physics 15, 5275–5303. doi:https://doi.org/10.5194/acp-15-5275-2015.

Intergovernmental Panel on Climate Change (IPCC), 2023. Sections. In: Climate Change 2023: Synthesis Report. Contribution of Working Groups I, II and III to the Sixth Assessment Report of the Intergovernmental Panel on Climate Change. IPCC. doi:10.59327/IPCC/AR6-9789291691647.

Jin, C., Xue, Y., Yuan, T., Zhao, L., Jiang, X., Sun, Y., Wu, S., Wang, X., 2024. Retrieval anthropogenic co2 emissions from oco-2 and comparison with gridded emission inventories. Journal of Cleaner Production 448, 141418. doi:https://doi.org/10.1016/j.jclepro.2024.141418.

Kuenen, J., Dellaert, S., Visschedijk, A., Jalkanen, J.P., Super, I., Denier van der Gon, H., 2022. Cams-reg-v4: A state-of-the-art high-resolution european emission inventory for air quality modelling. Earth System Science Data doi:https://doi.org/10.5194/essd-14-491-2022.

Landgraf, J., Borsdorff, T., Langerock, B., Keppens, A., 2023. S5p mission performance centre carbon monoxide readme. Netherlands: Netherlands Institute for Space Research [Last access Jan. 31, 2025].

Landgraf, J., de Brugh, J., Scheepmaker, R., Borsdorff, T., Houweling, S., Hasekamp, O., 2021. Algorithm theoretical baseline document for sentinel-5 precursor: Carbon monoxide total column retrieval. Netherlands: Netherlands Institute for Space Research .

Leguijt, G., Maasakkers, J.D., Denier van der Gon, H.A., Segers, A.J., Borsdorff, T., Aben, I., 2023. Quantification of carbon monoxide emissions from african cities using tropomi. Atmospheric Chemistry and Physics 23, 8899–8919. doi:https://doi.org/10.5194/acp-23-8899-2023.

Leguijt, G., Maasakkers, J.D., Denier van der Gon, H.A., Segers, A.J., Borsdorff, T., van der Velde, I.R., Aben, I., 2025. Comparing space-based to reported carbon monoxide emission estimates for europe's iron and steel plants. Atmospheric Chemistry and Physics 25, 555–574.

Lei, R., Feng, S., Danjou, A., Broquet, G., Wu, D., Lin, J.C., O'Dell, C.W., Lauvaux, T., 2021. Fossil fuel co2 emissions over metropolitan areas from space: A multi-model analysis of oco-2 data over lahore, pakistan. Remote Sensing of Environment 264, 112625. doi:https://doi.org/10.1016/j.rse.2021.112625.

Li, Y., Jiang, F., Jia, M., Feng, S., Lai, Y., Ding, J., He, W., Wang, H., Wu, M., Wang, J., et al., 2024. Improved estimation of co2 emissions from thermal power plants based on oco-2 xco2 retrieval using inline plume simulation. Science of The Total Environment 913, 169586. doi:https://doi.org/10.1016/j.scitotenv.2023.169586.

Molod, A., Takacs, L., Suarez, M., Bacmeister, J., Song, I.S., Eichmann, A., 2012. The GEOS-5 atmospheric general circulation model: Mean climate and development from MERRA to Fortuna. Technical Report. Accessed: 2024-12-21.

Nassar, R., Mastrogiacomo, J.P., Bateman-Hemphill, W., McCracken, C., MacDonald, C.G., Hill, T., O'Dell, C.W., Kiel, M., Crisp, D., 2021. Advances in quantifying power plant co2 emissions with oco-2. Remote Sensing of Environment 264, 112579. doi:https://doi.org/10.1016/j.rse.2021.112579.

NCEP, 2000. Ncep fnl operational model global tropospheric analyses. doi:https://doi.org/10.5065/D6M043C6.

Nelson, R.R., Cusworth, D.H., Thorpe, A.K., Kim, J., Elder, C.D., Nassar, R., Mastrogiacomo, J.P., 2024. Comparing near-simultaneous oco-3 and emit observations of co2 point sources from the iss. Authorea Preprints doi:10.22541/essoar.172296000.08268655/v1.

Nielsen, O.K., 2013. Emep/eea air pollutant emission inventory guidebook 2013. technical guidance to prepare national emission inventories .

Oda, T., Maksyutov, S., 2011. A very high-resolution (1 km× 1 km) global fossil fuel co 2 emission inventory derived using a point source database and satellite observations of nighttime lights. Atmospheric Chemistry and Physics 11, 543–556. doi:https://doi.org/10.5194/acp-11-543-2011.

Ohyama, H., Yoshida, Y., Matsunaga, T., 2024. Ch4 and co emission estimates for megacities: deriving enhancement ratios of co2, ch4, and co from gosat-2 observations. Environmental Research Letters doi:10.1088/1748-9326/ad89e0.

Park, H., Jeong, S., Park, H., Labzovskii, L.D., Bowman, K.W., 2021. An assessment of emission characteristics of northern hemisphere cities using spaceborne observations of co2, co, and no2. Remote Sensing of Environment 254, 112246. doi:https://doi.org/10.1016/j.rse.2020.112246.

Plant, G., Kort, E.A., Murray, L.T., Maasakkers, J.D., Aben, I., 2022. Evaluating urban methane emissions from space using tropomi methane and carbon monoxide observations. Remote Sensing of Environment 268, 112756. doi:https://doi.org/10.1016/j.rse.2021.112756.

Powers, J.G., Klemp, J.B., Skamarock, W.C., Davis, C.A., Dudhia, J., Gill, D.O., Coen, J.L., Gochis, D.J., Ahmadov, R., Peckham, S.E., et al., 2017. The weather research and forecasting model: Overview, system efforts, and future directions. Bulletin of the American Meteorological Society 98, 1717–1737. doi:https://doi.org/10.1175/BAMS-D-15-00308.1.

Scarpelli, T.R., Palmer, P.I., Lunt, M., Super, I., Droste, A., 2024. Verifying national inventory-based combustion emissions of co 2 across the uk and mainland europe using satellite observations of atmospheric co and co 2. Atmospheric Chemistry and Physics 24, 10773–10791. doi:https://doi.org/10.5194/acp-16-14371-2016.

Schneising, O., Buchwitz, M., Reuter, M., Weimer, M., Bovensmann, H., Burrows, J.P., Bösch, H., 2024. Towards a sector-specific co/co 2 emission ratio: Satellite-based observation of co release from steel production in germany. EGUsphere 2024, 1–17. doi:https://doi.org/10.5194/acp-24-7609-2024.

Sha, M.K., Langerock, B., Blavier, J.F.L., Blumenstock, T., Borsdorff, T., Buschmann, M., Dehn, A., De Mazière, M., Deutscher, N.M., Feist, D.G., et al., 2021. Validation of methane and carbon monoxide from sentinel-5 precursor using tccon and ndacc-irwg stations. Atmospheric Measurement Techniques 14, 6249–6304. doi:https://doi.org/10.5194/amt-14-6249-2021.

Sierk, B., Bézy, J.L., Löscher, A., Meijer, Y., 2019. The european co2 monitoring mission: observing anthropogenic greenhouse gas emissions from space, in: International Conference on Space Optics—ICSO 2018, SPIE. pp. 237–250. doi:https://doi.org/10.1117/12.2535941.

Smith, B., Wårlind, D., Arneth, A., Hickler, T., Leadley, P., Siltberg, J., Zaehle, S., 2014. Implications of incorporating n cycling and n limitations on primary production in an individual-based dynamic vegetation model. Biogeosciences 11, 2027–2054. doi:https://doi.org/10.5194/bg-11-2027-2014.

Taylor, T.E., Eldering, A., Merrelli, A., Kiel, M., Somkuti, P., Cheng, C., Rosenberg, R., Fisher, B., Crisp, D., Basilio, R., et al., 2020. Oco-3 early mission operations and initial (vearly) xco2 and sif retrievals. Remote Sensing of Environment 251, 112032. doi:https://doi.org/10.1016/j.rse.2020.112032.

Taylor, T.E., O'Dell, C.W., Baker, D., Bruegge, C., Chang, A., Chapsky, L., Chatterjee, A., Cheng, C., Chevallier, F., Crisp, D., et al., 2023. Evaluating the consistency between oco-2 and oco-3 xco 2 estimates derived from the nasa acos version 10 retrieval algorithm. Atmospheric Measurement Techniques Discussions 2023, 1–61. doi:https://doi.org/10.5194/amt-16-3173-2023.

Thorpe, A.K., Green, R.O., Thompson, D.R., Brodrick, P.G., Chapman, J.W., Elder, C.D., Irakulis-Loitxate, I., Cusworth, D.H., Ayasse, A.K., Duren, R.M., et al., 2023. Attribution of individual methane and carbon dioxide emission sources using emit observations from space. Science advances 9, eadh2391. doi:10.1126/sciadv.adh2391.

Varon, D.J., Jacob, D.J., McKeever, J., Jervis, D., Durak, B.O., Xia, Y., Huang, Y., 2018. Quantifying methane point sources from fine-scale satellite observations of atmospheric methane plumes. Atmospheric Measurement Techniques 11, 5673–5686. doi:https://doi.org/10.5194/amt-11-5673-2018.

Veefkind, J., Aben, I., McMullan, K., Förster, H., De Vries, J., Otter, G., Claas, J., Eskes, H., De Haan, J., Kleipool, Q., et al., 2012. Tropomi on the esa sentinel-5 precursor: A gmes mission for global observations of the atmospheric composition for climate, air quality and ozone layer applications. Remote sensing of environment 120, 70–83. doi:https://doi.org/10.1016/j.rse.2011.09.027.

Wang, W., Liu, X., Bi, J., Liu, Y., 2022. A machine learning model to estimate ground-level ozone concentrations in california using tropomi data and high-resolution meteorology. Environment International 158, 106917. doi:https://doi.org/10.1016/j.envint.2021.106917.

Wilmot, T.Y., Lin, J.C., Wu, D., Oda, T., Kort, E.A., 2024. Toward a satellite-based monitoring system for urban co2 emissions in support of global collective climate mitigation actions. Environmental Research Letters 19, 084029. doi:10.1088/1748-9326/ad6017.

Wu, D., Liu, J., Wennberg, P.O., Palmer, P.I., Nelson, R.R., Kiel, M., Eldering, A., 2022. Towards sector-based attribution using intra-city variations in satellite-based emission ratios between co 2 and co. Atmospheric Chemistry and Physics Discussions , 1–32doi:https://doi.org/10.5194/acp-22-14547-2022.

Wunch, D., Toon, G.C., Blavier, J.F.L., Washenfelder, R.A., Notholt, J., Connor, B.J., Griffith, D.W., Sherlock, V., Wennberg, P.O., 2011. The total carbon column observing network. Philosophical Transactions of the Royal Society A: Mathematical, Physical and Engineering Sciences 369, 2087–2112. doi:https://doi.org/10.1098/rsta.2010.0240.

Yang, E.G., Kort, E.A., Ott, L.E., Oda, T., Lin, J.C., 2023. Using space-based co2 and no2 observations to estimate urban co2 emissions. Journal of Geophysical Research: Atmospheres 128, e2022JD037736. doi:https://doi.org/10.1029/2022JD037736.

Yang, Y., Zhou, M., Wang, W., Ning, Z., Zhang, F., Wang, P., 2024. Quantification of co2 emissions from three power plants in china using oco-3 satellite measurements. Advances in Atmospheric Sciences , 1–13doi:https://doi.org/10.1007/s00376-024-3293-9.

Ye, X., Lauvaux, T., Kort, E.A., Oda, T., Feng, S., Lin, J.C., Yang, E.G., Wu, D., 2020. Constraining fossil fuel co2 emissions from urban area using oco-2 observations of total column co2. Journal of Geophysical Research: Atmospheres 125, e2019JD030528. doi:https://doi.org/10.1029/2019JD030528.

Zhang, Q., Boersma, K.F., Zhao, B., Eskes, H., Chen, C., Zheng, H., Zhang, X., 2023. Quantifying daily no x and co2 emissions from wuhan using satellite observations from tropomi and oco-2. Atmospheric Chemistry and Physics 23, 551–563. doi:https://doi.org/10.5194/acp-23-551-2023.